Control of Bering Strait Transport by the Meridional Overturning Circulation

PAOLA CESSI

Scripps Institution of Oceanography, University of California, San Diego, La Jolla, California

(Manuscript received 30 January 2020, in final form 22 March 2020)

ABSTRACT

It is well established that the mean transport through Bering Strait is balanced by a sea level difference between the North Pacific and the Arctic Ocean, but no mechanism has been proposed to explain this sea level difference. It is argued that the sea level difference across Bering Strait, which geostrophically balances the northward throughflow, is associated with the sea level difference between the North Pacific and the North Atlantic/Arctic. In turn, the latter difference is caused by deeper middepth isopycnals in the Indo-Pacific than in the Atlantic, especially in the northern high latitudes because there is deep water formation in the Atlantic, but not in the Pacific. Because the depth of the middepth isopycnals is associated with the dynamics of the upper branch of the meridional overturning circulation (MOC), a model is formulated that quantitatively relates the sea level difference between the North Pacific and the Arctic/North Atlantic with the wind stress in the Antarctic Circumpolar region, since this forcing powers the MOC, and with the outcropping isopycnals shared between the Northern Hemisphere and the Antarctic circumpolar region, since this controls the location of deep water formation. This implies that if the sinking associated with the MOC were to occur in the North Pacific, rather than the North Atlantic, then the Bering Strait flow would reverse. These predictions, formalized in a theoretical box model, are confirmed by a series of numerical experiments in a simplified geometry of the World Ocean, forced by steady surface wind stress, temperature, and freshwater flux.

1. Introduction

Bering Strait connects the North Pacific and Arctic Oceans at about 66°N: with an average depth of 50 m and a minimum width of 85 km, its climatologically averaged transport is northward (from the Pacific into the Arctic) and about 0.8 Sv (1 Sv $\equiv 10^6\,\mathrm{m^3\,s^{-1}}$)—increased to 1 Sv for the period 2003–15—with seasonal minimum in winter of 0.5 Sv and maximum in summer of 1.5 Sv (Woodgate 2018). The seasonal modulation of the transport is correlated with the local wind, south-westward and strong in winter and weak in summer, which tends to drive the flow toward the south. Occasionally the wind reverses the flow, and the transport becomes opposite to the climatological direction.

The net northward flow is geostrophically balanced by a pressure and sea surface height (SSH) difference between the western and eastern sides of the strait (Toulany and Garrett 1984; Panteleev et al. 2010; Woodgate 2018) of about 0.2 m. This SSH difference is due to two processes: 1) the along-strait wind stress is frictionally balanced by an along strait velocity (southward), which is in geostrophic balance with the across-strait SSH difference, and 2) a large-scale pattern of SSH, with the North Pacific standing higher than the Arctic and the North Atlantic. In the twenty-first century, the locally wind-driven SSH difference produces an average transport of about −0.1 Sv, while the SSH difference between the North Pacific and the Arctic produces an average transport of about 1.1 Sv (Woodgate 2018). Here the focus is on the latter process, which accounts for the sign and magnitude of the climatological Bering Strait transport.

Detailed observations show that the Bering Strait transport associated with the SSH difference between the North Pacific and the Arctic has little seasonal variation (Aagaard et al. 2006; Woodgate 2018), in contrast with the component associated with the local wind stress. Given the large seasonal cycle of the atmospheric conditions in this high-latitude region, the weak seasonality suggests that this component of the SSH is not determined by local processes. Figure 1 shows the climatological SSH anomalies from a comprehensive reanalysis of global observations (Forget et al. 2015; Fukumori et al. 2017). Representative values are in the high-latitude North Pacific at 60°N and 165°W, SSH = 0.19 m, and in the high-latitude North Atlantic at 60°N

Corresponding author: Paola Cessi, pcessi@ucsd.edu

DOI: 10.1175/JPO-D-20-0026.1

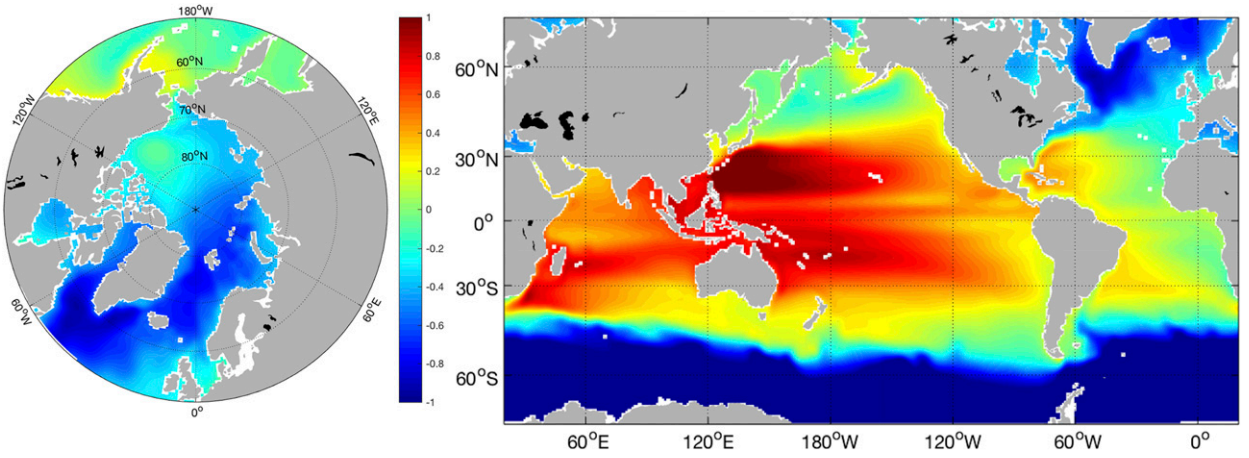

FIG. 1. Time-averaged sea level (SSH) anomaly from ECCO4 (Forget et al. 2015; Fukumori et al. 2017): (left) a polar view and (right) a Mercator-projection global view. The color bar is the same for the two panels, and the units are in meters.

and 5°E, SSH = −0.43 m, resulting in an SSH difference of about 0.6 m. This difference is larger by a factor of 3 than the typical difference between the South Pacific and South Atlantic basins. For example, at 30°S and 72°W the SSH is 0.12 m, while at 30°S and 16°E it is −0.12 m. Thus, the SSH difference that balances the climatological northward flow at Bering Strait has large spatial and long time scales and is part of the global ocean circulation, rather than a regional phenomenon. It is noteworthy that the variation in SSH along the eastern boundary of the Pacific is smaller than on the eastern boundary of the Atlantic.

Indeed, regional models of the North Pacific–Arctic region require the prescription of SSH, temperature and salinity and, in some cases, velocities at their outer open boundaries in order to properly simulate the Bering transport (Zhang et al. 2010; Nguyen et al. 2011; Danielson et al. 2011). Another regional model, with closed outer boundaries at 30°N, achieves a pressure difference between the Atlantic and Pacific by blowing a $0.175\,\mathrm{N\,m^{-2}}$ westward wind stress along an artificial channel that crosses the North American continent from coast to coast at 30°N (Maslowski et al. 2004; Kinney et al. 2014). Other regional models that do not include remote SSH differences or inflow–outflow at the outer boundaries can simulate the anomalies of Bering Strait transport, but not its climatological mean: Danielson et al. (2014) shows that local wind and sea level pressure forcing and shelf waves dynamics account for about half of the transport variability, but produce near-zero climatological Bering Strait transport.

Perhaps counterintuitively, a comparison of four regional and one global model shows that the climatological transport and temperature distribution at Bering Strait is represented better in a model with only three grid points across the strait than in models with higher resolution (Kinney et al. 2014). Additionally, the state estimate provided at 1° resolution by Estimating the Circulation and Climate of the Ocean (version 4, release 3; ECCO4) has 1 Sv going through Bering Strait with a single grid point at the strait (the Bering Strait transport *is not* a constraint assimilated in ECCO4) (Forget et al. 2015; Fukumori et al. 2017). These modeling results provide additional evidence that the climatological transport is not controlled by geographically local processes.

The body of observations and simulations summarized above clarify that the SSH difference between the North Pacific and the Arctic/North Atlantic is essential to dynamically balance the climatological transport through Bering Strait. Thus, in order to understand the control of the time-mean Bering Strait throughflow, the time-mean SSH difference mentioned above must be explained.

Almost 60 years ago Reid (1961) documented an observed difference in SSH between the Pacific and Atlantic, relative to 1000 dbar. A convincing dynamical theory for this difference was provided only recently by Jones and Cessi (2016) and Thompson et al. (2016): the ageostrophic transport entering the upper waters (above about 1000 m) of the Indo-Pacific sector from the Southern Ocean must exit this sector in the Southern Hemisphere and enter the Atlantic sector where it eventually sinks to form North Atlantic Deep Water (NADW). This interbasin transport is geostrophically balanced by a difference in pressure between the eastern boundaries of the South Pacific and South Atlantic, which manifests itself as a difference in SSH and in isopycnal depths. Numerical experiments show that when deep water formation moves from the North

Atlantic to the North Pacific (by manipulating the freshwater fluxes in the northern high latitudes of the basins), the SSH and pressure difference between the Pacific and Atlantic changes sign, i.e., SSH is higher in the Atlantic than in the Pacific (Hu et al. 2011; Jones and Cessi 2016; Cessi and Jones 2017). Thus, the interbasin Pacific–Atlantic SSH difference is associated with the localization of the meridional overturning circulation (MOC).

A series of numerical experiments where the Atlantic MOC (AMOC) is weakened by the addition of freshwater in the Arctic (Hu and Meehl 2005; Hu et al. 2008, 2011) further shows that the location of deep water formation controls the climatological Bering Strait transport (Hu and Meehl 2005; Hu et al. 2008, 2011). The Bering Strait transport weakens with the AMOC, and even reverses when the AMOC collapses. In the AMOC-collapsed state the Bering Strait transport is -1 Sv, i.e., equal and opposite to the value in the unperturbed, AMOC-on control case, and SSH is higher in the Atlantic/Arctic relative to the Pacific (Hu et al. 2011).

Despite the evidence from observations and results from comprehensive ocean models showing the global control of the SSH difference and flow through Bering Strait, no conceptual framework has been put forward to explain the connection between the global overturning circulation, large-scale SSH differences and the Bering Strait throughflow.

The only relevant study is De Boer and Nof (2004) who considered the momentum, volume, temperature, and salinity budgets of the Atlantic. The momentum budget uses "Godfrey's island rule" (Godfrey 1989) for the AMOC's upper branch with the American continent as the "island." assuming that the pressure is constant all along the eastern boundaries of the Atlantic and Indo-Pacific basins. This assumption is problematic for the Atlantic because in the sinking region mixing is large and the pressure is no longer constant along the eastern boundary (Sumata and Kubokawa 2001). Indeed, the outcropping of isopycnals associated with NADW production is a central element to the theoretical framework for the climatological Bering Strait transport offered here. In addition, De Boer and Nof (2004) neglect the baroclinic form stress between the tips of South Africa and South America associated with eddy transport and the diapycnal upwelling, which are important contributors to the AMOC.

In the following we build a conceptual model that relates the SSH difference across Bering Strait, and the associated transport, to the meridional overturning circulation. The predictions of the theory are tested against numerical solutions of the primitive equations in a simplified configuration of the World Ocean. The goal of these simplified models is not to simulate the detailed features of the circulation in the Bering Strait and its surrounding region, but rather to understand the important process that maintains the climatological SSH difference and transport across Bering Strait against the local wind stress and friction, both of which tend to oppose the northward flow. Thus, we quantify how the *sign and magnitude* of the SSH difference across the strait is related to the global middepth overturning circulation. This is a complementary approach to that of the regional models summarized in Kinney et al. (2014), which impose this SSH difference at the outer boundary of the domain.

2. Conceptual model

The essential element of the theory is that the SSH difference across Bering Strait is dominated by the large-scale difference in sea level associated with outcropping of dense isopycnals in the North Atlantic, but not in the North Pacific. This North Atlantic outcropping marks the sinking region of the MOC and the formation of NADW, and is absent in the Indo-Pacific.

The pressure difference across Bering Strait can be determined by assuming that the velocities are geostrophically balanced, and thus pressure and SSH are constant all along the uninterrupted portions of the Pacific northern boundary and the Arctic southern boundaries. In this way, the pressure and SSH at the eastern (western) boundary of Bering Strait are given by the pressure and SSH at the northeast corner of the Pacific (Atlantic) basin. In turn, the pressure and SSH along the eastern boundary of the Pacific basin (including the northeast corner) is geostrophically balanced, and thus constant, and determined at the southeast corner of the Pacific basin.

The Pacific basin eastern boundary pressure is quantified using the buoyancy, mass and momentum budget of the upper limb of the MOC, which involves consideration of the global ocean, including the Atlantic, Indo-Pacific, and Southern Ocean sectors (Cessi 2019; Johnson et al. 2019). In the spirit of Gnanadesikan (1999), Jones and Cessi (2016), and Cessi and Jones (2017), the budget is performed above an isopycnal of depth h, i.e., the depth of the densest isopycnal that outcrops on the eastern boundary of the North Atlantic, where NADW forms. The isopycnal of depth h approximately separates the upper and lower limbs of the MOC, and it is called "separating depth" henceforth: typical values for h are 1200 m, much deeper than the depth of the subtropical thermocline. A further simplification is to combine all the density classes above the separating depth into an average value ρ_1, and all the density classes below $z = -h$ into an average value ρ_o.

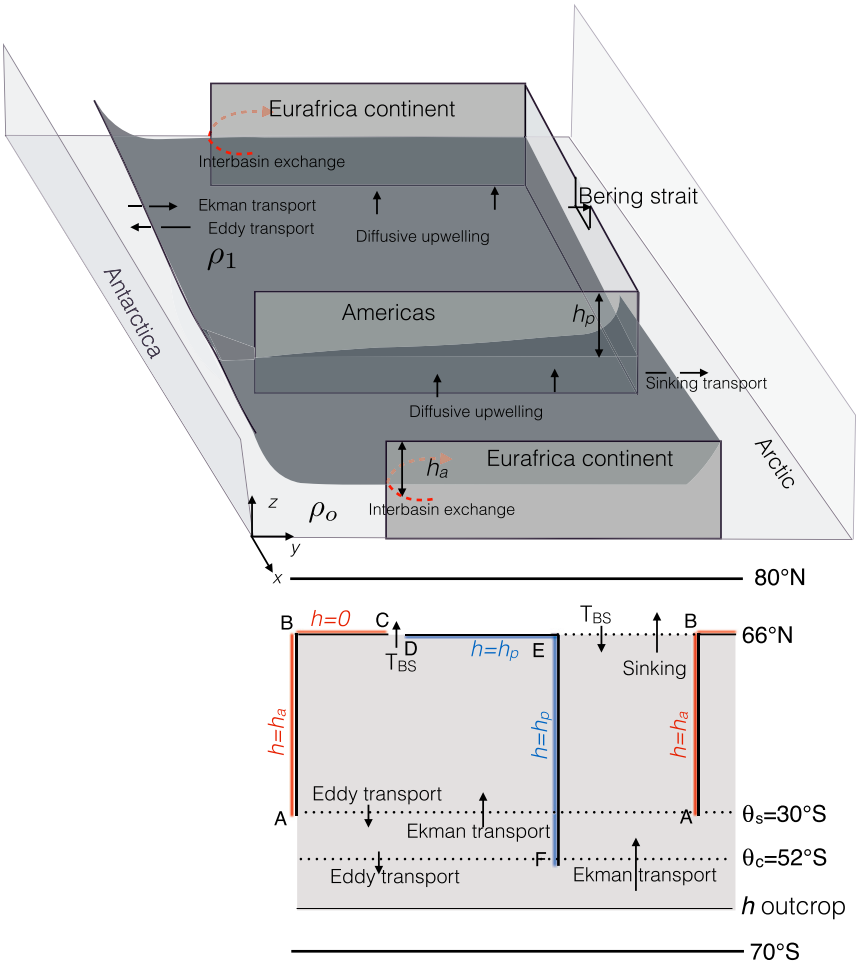

FIG. 2. Geometry of the conceptual model illustrating the buoyancy budget for the residual circulation above the isopycnal separating the upper and lower limb of the middepth MOC when sinking is in the Atlantic-like (narrow) basin: (top) 3D view and (bottom) 2D view showing the latitudes of solid boundaries. Pressure and SSH are constant along the segments B–C and D–E, and equal to the values at point B and E, respectively.

With reference to Fig. 2, the sources and sinks of buoyancy above the separating isopycnal of depth h are shown. The quantitative budget is expressed in terms of two unknowns, h_a and h_p, which are the constant values of h at the eastern boundary of the Atlantic-like basin (narrow) and of the Pacific-like basin (wide), respectively. The important point is that h is constant and has the value h_p all along the west coast of the American continent, i.e., the eastern boundary of the Pacific-like basin, while h vanishes near the latitudes separating the North Atlantic and the Arctic, i.e., near the northeast corner of the Atlantic Basin.

The buoyancy budget just described provides the pressure and SSH at the northeast boundaries of the North Atlantic and North Pacific. Assuming further that the pressure and SSH are geostrophically balanced and thus constant along the northern boundary of the Pacific and the southern boundary of the Arctic, the SSH and pressure can be determined at the eastern and western sides of Bering Strait.

a. *Relating the SSH at Bering Strait to h*

The flow through Bering Strait is assumed to be in geostrophic balance, and thus proportional to $p_e - p_w$, where p_e and p_w are the pressures on the eastern and western sides of the strait, respectively. Because of the shallowness of strait, the pressure difference $p_e - p_w$ can be considered independent of depth. The pressure can be calculated using the linear free surface approximation (Gill and Niller 1973):

$$p(x,y,z,t) = p_{\text{atm}}(x,y,t) + \rho_o g\eta(x,y,t) - \int_z^0 g\rho(x,y,z',t)\,dz', \quad (1)$$

where $p_{\rm atm}$ is the sea level pressure (SLP), η is the SSH, g is the gravitational acceleration, and ρ_o is the Boussinesq reference pressure. Evaluating (1) at $z = 0$, the height of the geoid, we obtain that the pressure difference across Bering Strait is given by

$$p_e - p_w = \Delta p_{\rm atm} + \rho_o g \Delta\eta, \tag{2}$$

where

$$\Delta\eta \equiv \eta(x_E, 66°\text{N}) - \eta(x_W, 66°\text{N}) \tag{3}$$

is the SSH difference across Bering Strait and $\Delta p_{\rm atm}$ is the atmospheric pressure difference. The latter will be neglected henceforth, assuming that the climatological atmospheric pressure has a horizontal scale much larger than the strait width. Thus, the geostrophically balanced Bering Strait transport $T_{\rm BS}$ is given by

$$T_{\rm BS} = H_{\rm BS}\frac{g\Delta\eta}{f_{\rm BS}}, \tag{4}$$

where $H_{\rm BS}$ is the depth of Bering Strait, considered constant, and $f_{\rm BS}$ is the Coriolis parameter at 66°N.

We now assume that the pressures p_e and p_w at $z = 0$ are constant along uninterrupted solid boundaries because of geostrophy, so they can be calculated at the northern edge of the eastern boundaries of the North Pacific and North Atlantic, respectively. With reference to the lower panel of Fig. 2, we assume that the pressure and η are constant along the segment D–E and along the segment B–C, so that p_e is the pressure at $z = 0$ of point E (the northeast corner of the Pacific basin) and p_w is the pressure at $z = 0$ of point C (the northeast corner of the Atlantic basin).

In the basin regions, the SSH can be related to the depth h using the one-and-a-half layer approximation of (1):

$$g\eta(x,y,t) = -\frac{p_{\rm atm}(x,y,t)}{\rho_o} + \frac{p_o}{\rho_o} + g\frac{\rho_o - \rho_1}{\rho_o}h(x,y,t), \tag{5}$$

where p_o is the constant pressure below $z = -h$.

Neglecting $p_{\rm atm}$, the SSH difference across Bering Strait $\Delta\eta$ is given by

$$g\Delta\eta \approx g' h_p, \tag{6}$$

where $g' \equiv g(\rho_o - \rho_1)/\rho_o$ is the range of surface buoyancies shared between the Antarctic circumpolar region and the region of deep water formation in the Northern Hemisphere (Wolfe and Cessi 2010). Because there is no deep water formation in the Pacific, the geostrophic pressure and η are constant on the arclength comprising the eastern boundary of the Pacific basin and the eastern half of the northern boundary of the Pacific, so along this arclength $g\eta = p_o/\rho_o + g' h_p$. Similarly, because the interface outcrops at the northern edge of the eastern boundary of the North Atlantic, the SSH all along the western half of the northern solid boundary of the Pacific (on the Arctic side) is $g\eta = p_o/\rho_o$. Unlike the pressure and separating depth in the Pacific h cannot be considered constant all along the arclength of the eastern boundary of the Atlantic: in the deep water formation region mixing becomes important and at the northeast corner of the Atlantic basin $h = 0$, while it has a finite value $h = h_a$ along the eastern boundary away from the mixing region.

An implicit assumption of the theory is the neglect of friction and any along-coast wind stress on the boundary arclength, which would modify the pressure and thus the SSH along the boundaries' arclengths.

It is now possible to directly relate the Bering Strait transport $T_{\rm BS}$ to h_p, through the geostrophic relation

$$T_{\rm BS} = H_{\rm BS}\frac{g' h_p}{f_{\rm BS}}. \tag{7}$$

The local wind stress is neglected in (7), because we focus on the large-scale, rather than local, SSH signal. Similarly, friction is neglected, even though it presumably has some influence in such a narrow and shallow strait (Stigebrandt 1984).

With reference to Fig. 2, we can now evaluate h_p by considering the buoyancy budget of two regions between $z = -h$ and the sea surface: the global domain north of 52°S, and the Pacific-like subdomain north of 30°S.

b. *The buoyancy budget above the separating depth h*

In the following we derive the details of the model. In summary, the MOC is powered by the Ekman transport in the circumpolar region, taken at its maximum, i.e., at the subpolar/subtropical boundary of the Southern Ocean. The steepening of the outcropping isopycnal due to the Ekman cell in the circumpolar region is counteracted by eddy fluxes of buoyancy (Gnanadesikan 1999; Marshall and Radko 2003), parameterized as diffusion of isopycnal thickness, with constant eddy diffusivity $\kappa_{\rm GM}$ (Gent and McWilliams 1990; Griffies 1998): the slope of the isopycnal is then approximated to be linear between the latitude of interest and the outcrop latitude in the southern circumpolar region.

The goal of the conceptual model is to express the buoyancy budget in term of two unknowns, i.e., the constant values of the separating depth at the eastern boundaries of the basins h_p and h_a, given the values of the external parameters that characterize the wind stress, the surface buoyancy and the geometry of the domain. We derive two equations in the two unknowns h_p and h_a using the momentum, buoyancy, hydrostatic

and continuity equations, following Gnanadesikan (1999) and Jones and Cessi (2016).

Although h vanishes in the sinking region, it has a finite depth elsewhere and the Atlantic-like (narrow) basin participates in the global buoyancy budget, primarily by hosting the sinking associated with the MOC. In the following, we denote with h_a the constant value of the isopycnal depth on the eastern side of the Atlantic-like basin away from the sinking region, and we use (6) for the evaluation of the geostrophically balanced Bering Strait transport.

The buoyancy budget can be obtained by integrating the continuity equation, $\nabla \cdot \mathbf{v} = 0$, above the separating depth $z = -h$ in the vertical and over the area of the domain of interest in the horizontal, i.e.,

$$\int_A da \int_{-h}^{0} \nabla \cdot \mathbf{v}\, dz = 0, \tag{8}$$

where $\mathbf{v} \equiv (u, v, w)$ is the three-dimensional velocity vector in depth coordinates and A is the horizontal area of the domain of interest. The integrated continuity equation can also be written as

$$\nabla \cdot \int_A \mathbf{u} h\, da + \int_A (E - P - R + \eta_t + h_t - \varpi)\, da = 0, \tag{9}$$

where $\mathbf{u}$ is the vertically averaged horizontal velocity, $E - P - R$ is (minus) the net surface freshwater flux, ϖ is the diapycnal velocity across $z = -h$, and h_t and η_t are the tendency of h and η, respectively. The tendency terms vanish when considering the climatological average, and the freshwater flux is neglected henceforth. Performing the integral over longitude on the first term of (9) in a domain either bounded by solid walls or periodic in longitude removes the dependence on the zonal component of the velocity leaving the following terms

$$L_x(\overline{v}\,\overline{h} + \overline{v'h'})\Big|_{\text{South}}^{\text{North}} - \int_A \varpi, da = 0, \tag{10}$$

where $\overline{v}$ and $\overline{h}$ are the meridional velocity and separating depth, respectively, zonally averaged over the longitudinal width L_x, and $\overline{v'h'}$ is the meridional transport of thickness associated with waves and eddies, zonally averaged over L_x. These quantities are evaluated at the southern and northern boundaries of the domain of interest.

With reference to the lower panel of Fig. 2, we first consider the domain bounded by $\theta_c = 52°$S and $\theta = 66°$N in latitude and comprising all longitudes. Because of the circumpolar geometry at θ_c, there is no zonally averaged geostrophic meridional transport and $\overline{v}\,\overline{h}|_{\theta_c} = -\tau_c/(\rho_o f_c)$, i.e., the ageostrophic Ekman transport at 52°S. We parameterize the eddy thickness transport following Gent and McWilliams (1990), so that $\overline{v'h'} = -\kappa_{\text{GM}} \overline{h}_y$, with κ_{GM} constant. Assuming that the slope of the isopycnal is linear in the circumpolar region we get $\overline{h}_y|_{\theta_c} = \overline{h}|_{\theta_c}/L_c$, where L_c is the meridional distance between the Southern Hemisphere outcrop and θ_c. We then identify $\overline{h}|_{\theta_c}$ with h_p.

There are two terms associated with the area-integrated diapycnal velocity at the separating depth $z = -h$: the diffuse upwelling due to diapycnal mixing and the sinking due to NADW formation. To estimate the mixing term, we use scale analysis, while the sinking term is equal to (the negative of) the zonal integral of the geostrophically balanced meridional transport in the upper branch of the AMOC just south of the outcrop. Thus, we have

$$\int_A \varpi\, da = \underbrace{\frac{\kappa A_a}{h_a} + \frac{\kappa A_p}{h_p}}_{\text{Diffusive}} - \underbrace{g' \frac{h_a^2 - h_w^2}{2 f_{\text{BS}}}}_{\text{Sinking}}, \tag{11}$$

where κ is the diapycnal diffusivity; A_a, A_p are the areas of the Atlantic and Indo-Pacific sectors respectively; and h_w is the depth of the isopycnal interface on the western boundary of the North Atlantic sector just south of the outcrop. In this subpolar region h_w is much smaller than h_a, and can be neglected. In other words, sinking is assumed to occur at a lower latitude on the western boundary relative to the eastern boundary.

In summary, the global buoyancy budget in the region between 52°S and 66°N and above the separating depth can be expressed as

$$\underbrace{-\frac{\tau_c L}{\rho_o f_c}}_{\text{Ekman}} \underbrace{-\frac{\kappa_{\text{GM}} h_p L}{L_c}}_{\text{Eddy}} + \underbrace{\frac{\kappa A_a}{h_a} + \frac{\kappa A_p}{h_p}}_{\text{Diffusive}} = \underbrace{g' \frac{h_a^2}{2 f_{\text{BS}}}}_{\text{Sinking}}. \tag{12}$$

A second relation is obtained considering the buoyancy budget above the separating depth in the Indo-Pacific sector between 30°S and 66°N. In addition to terms analogous to those entering the global budget, we must also consider a geostrophically balanced interbasin meridional transport at 30°S, given by $g'(h_p^2 - h_a^2)/(2 f_s)$, as well as the transport through Bering Strait, both exchanged between the Atlantic and the Indo-Pacific basins. The budget in the Indo-Pacific gives

$$\underbrace{-\frac{\tau_s L_p}{\rho_o f_s}}_{\text{Ekman}} \underbrace{-\frac{\kappa_{\text{GM}} h_p L_p}{L_s}}_{\text{Eddy}} + \underbrace{\frac{\kappa A_p}{h_p}}_{\text{Diffusive}} + \underbrace{\frac{g'(h_p^2 - h_a^2)}{2 f_s}}_{\text{Interbasin}} = \underbrace{H_{\text{BS}} \frac{g' h_p}{f_{\text{BS}}}}_{T_{\text{BS}}}, \tag{13}$$

where the definition and typical values of the symbols used in (12) and (13) are given in Table 1.

The are several differences between our approach and that of De Boer and Nof (2004): in our approach the

TABLE 1. Standard values of the parameters used in the conceptual model of (12) and (13).

Parameter	Value	Notes
θ_s	30°S	Latitude of tip of Eurafrican continent
θ_c	52°S	Latitude of subpolar/subtropical intergyre boundary
f_s	$-7.3\times10^{-5}\,\mathrm{s}^{-1}$	Coriolis parameter at θ_s
f_c	$-9.9\times10^{-5}\,\mathrm{s}^{-1}$	Coriolis parameter at θ_c
f_{BS}	$1.2\times10^{-4}\,\mathrm{s}^{-1}$	Coriolis parameter at Bering Strait
τ_s	$4.3\times10^{-2}\,\mathrm{Pa}$	Wind stress at θ_s
τ_c	0.2 Pa	Wind stress at θ_c
L_p	$1.3\times10^{7}\,\mathrm{m}$	Width of the wide basin at θ_s
L	$1.7\times10^{7}\,\mathrm{m}$	Width of the Southern circumpolar basin at θ_c
L_c	$3.1\times10^{6}\,\mathrm{m}$	Distance between θ_c and h outcrop in Southern Ocean
L_s	$4.4\times10^{6}\,\mathrm{m}$	Distance between θ_s and h outcrop in Southern Ocean
A_a	$8.8\times10^{13}\,\mathrm{m}^2$	Area of the narrow basin
A_p	$1.4\times10^{14}\,\mathrm{m}^2$	Area of the wide basin
H_{BS}	67 m	Mean depth of the Bering strait
ρ_o	$1000\,\mathrm{kg\,m}^{-3}$	Boussinesq reference density
κ	$2\times10^{-5}\,\mathrm{m}^2\,\mathrm{s}^{-1}$	Diapycnal diffusivity
κ_{GM}	$500\,\mathrm{m}^2\,\mathrm{s}^{-1}$	Coefficient of eddy parameterization
g'	$5.9\times10^{-3}\,\mathrm{m\,s}^{-2}$	Reduced gravity

SSH on the western side of Bering Strait takes into account the outcropping of the middepth isopycnals in the North Atlantic associated with NADW formation, while the treatment of the SSH on the eastern side of the strait coincides in the two theories; we include the transport of buoyancy by eddies in the Southern Ocean, appropriately parameterized, and the diapycnal mixing at the interface depth, while these effects are neglected in De Boer and Nof (2004); we give explicit expressions for the different terms contributing to the buoyancy budget in terms of the eastern boundary pressures, h_a and h_p, using the approximate momentum balance.

The algebraic coupled system (12) and (13) is easily solved numerically for h_a and h_p, but it is useful to calculate an approximate solution valid for wind stress in the range of the Southern Ocean westerlies, i.e.,

$$h_a \approx \sqrt{-\frac{2f_{\mathrm{BS}}\tau_c L}{g'\rho_o f_c}}, \quad h_p \approx \sqrt{-\frac{2f_{\mathrm{BS}}\tau_c L}{g'\rho_o f_c}+\frac{2\tau_s L_p}{g'\rho_o}}. \tag{14}$$

Figure 3 shows the dependence of h_a and h_p as a function of the amplitude of the wind stress, measured by the maximum westerly wind stress in the Southern Ocean, for the parameter values given in Table 1. The important points are 1) the depth of the isopycnal bounding the upper limb of the MOC from below increases as the square root of the wind stress in the Southern Ocean (Gnanadesikan 1999), except for small values of the wind stress, in which case the eddy transport and diapycnal terms become important; 2) $h_p > h_a$ so that the interbasin exchange, proportional to $(h_p^2 - h_a^2)/f_s$, is negative (recall that $f_s < 0$), i.e., from the Pacific-like basin into the Atlantic-like basin (Jones and Cessi 2016; Cessi and Jones 2017). As advertised, the middepth isopycnals are deeper in the Pacific than Atlantic and the SSH is higher in the Pacific than Atlantic, as observed by Reid (1961).

The corresponding values for the Bering Strait transport T_{BS} as a function of the amplitude of the wind stress are shown in Fig. 4, for the parameter values given in Table 1. For the oceanographically relevant range of $\tau_c = 0.1$–0.2 Pa the geostrophically balanced Bering Strait transport is 2.5–3.2 Sv, i.e., about 2–3 times larger than observations. As shown in section 3 these predictions are correct given the geometry of the domain, which neglects the Arctic shelf, and the wind stress at the latitude of Bering Strait.

Another prediction of the model is that the flow through Bering Strait should reverse if sinking were to occur in the Pacific-like basin. Figure 5 shows the geometry of the isopycnal separating the upper and lower limb of the overturning in this case: the isopycnal vanishes at the latitude of Bering Strait on the Pacific (east) side ($h_p = 0$ at the latitude of Bering Strait), rather than on the Atlantic (west) side. Thus, the Bering Strait transport is now given by

$$T_{\mathrm{BS}} = -H_{\mathrm{BS}}\frac{g'h_a}{f_{\mathrm{BS}}}, \tag{15}$$

and the transport is negative (southward). The depth of the isopycnal, measured by h_a and h_p, is now governed by

$$\underbrace{-\frac{\tau_c L}{\rho_o f_c}}_{\text{Ekman}} \underbrace{-\frac{\kappa_{\mathrm{GM}} h_p L}{L_c}}_{\text{Eddy}} + \underbrace{\frac{\kappa A_a}{h_a}+\frac{\kappa A_p}{h_p}}_{\text{Diffusive}} = \underbrace{g'\frac{h_p^2}{2f_{\mathrm{BS}}}}_{\text{Sinking}}, \tag{16}$$

and

$$\underbrace{-\frac{\tau_s L_p}{\rho_o f_s}+\frac{\tau_c L}{\rho_o f_c}}_{\text{Ekman}} \underbrace{-\frac{\kappa_{\mathrm{GM}} h_p L_p}{L_s}+\frac{\kappa_{\mathrm{GM}} h_p L}{L_c}}_{\text{Eddy}} \underbrace{-\frac{\kappa A_a}{h_a}}_{\text{Diffusive}} + \underbrace{\frac{g'(h_p^2-h_a^2)}{2f_s}}_{\text{Interbasin}} = \underbrace{-H_{\mathrm{BS}}\frac{g'h_a}{f_{\mathrm{BS}}}}_{T_{\mathrm{BS}}}. \tag{17}$$

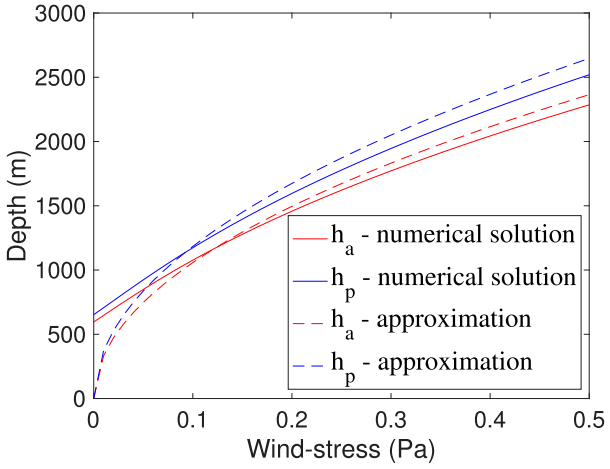

FIG. 3. Approximate (dashed) and numerical (solid) solutions of the system (16) and (17) for the parameter values given in Table 1.

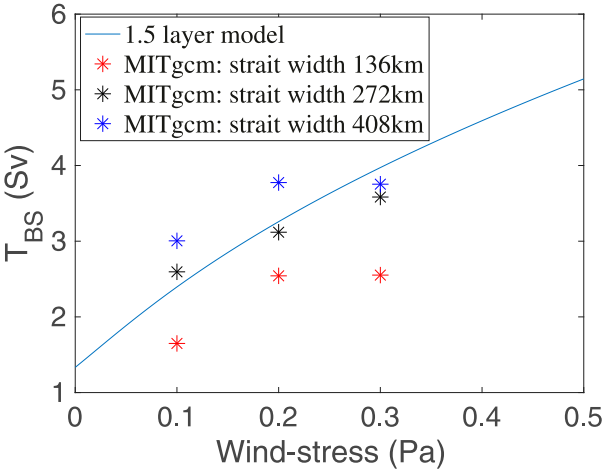

FIG. 4. The transport across the strait using (7) with h_p obtained from the numerical solution of the system (16) and (17) for the parameter values given in Table 1 (solid line). The star markers show the transport across the strait for the primitive equation computations (MITgcm) for different widths of the strait and amplitude of the westerly wind stress maximum in the Southern Hemisphere.

In this case the approximate solution of (16) and (17), valid for oceanographically relevant wind stress is

$$h_p \approx \sqrt{-\frac{2f_{\mathrm{BS}}\tau_c L}{g'\rho_o f_c}}, \quad h_a \approx \sqrt{-\frac{2\tau_c L}{g'\rho_o f_c}(f_{\mathrm{BS}} - f_s) - \frac{2\tau_s L_p}{g'\rho_o}}. \tag{18}$$

As before, the numerical solution of (16) and (17) agrees with the approximation (18) (figure not shown). The important point is that, to a first approximation, the Bering Strait transport is proportional to the square root of the wind stress in the Southern Hemisphere. This dependence is mediated by the depth of isopycnal separating the upper and lower limbs of the MOC in the nonsinking basin, which is directly proportional to the SSH difference between the North Pacific and the Atlantic at the latitudes of the Bering Strait.

In the following, the predictions of the conceptual model are tested against solutions of the primitive equations in a simple geometrical configuration of the World Ocean, forced by simplified wind stress, temperature, and freshwater fluxes, all prescribed at the surface.

3. Results of a general circulation model

The predictions and assumptions of the conceptual model are tested in an ocean general circulation model (GCM), configured in an idealized global ocean geometry, as illustrated in Fig. 6. The model is the MITgcm (Marshall et al. 1997) which solves the discretized primitive equations in a spherical sector 210° wide with solid boundaries to the south at 70°S and to the north at 80°N. The domain is divided into semi-enclosed subbasins separated by boundaries along the meridians at 0° and 70°E. The narrow, Atlantic-like subbasin is 70° wide and has solid boundaries extending from 52°S to 66°N at 0°E, representing the American (long) continent, and 30°S to 66°N at 70°E, representing the Eurafrican (short) continent. Both basins are open on the south to a region 210°-periodic in longitude, which represents the Antarctic circumpolar region. In addition, the narrow basin opens on the north to a region 210°-periodic in longitude representing the Arctic Ocean. The wide, Pacific-like subbasin is closed to the north at 66°N, except for a Bering-like strait that is 67 m deep and whose width is varied among solutions between 0 (closed strait), 136 (single strait), 272 (double strait), and 408 km (triple strait). The model narrowest strait is almost twice as wide as Bering Strait, and is resolved by three grid points in longitude, the minimum needed to calculate the gradients of tracers and velocity.

Elsewhere, the domain is 4000 m deep, except that south of the long continent there is a ridge 2000 m high and 1° wide in longitude. The model's resolution is 1° in latitude and longitude. In the vertical direction there are 32 unequally spaced levels with depths ranging from 6.8 m near the surface to 143 m at the bottom. The equation of state is taken to be linear with thermal and haline expansion coefficients equal to $2 \times 10^{-4}\,\mathrm{K}^{-1}$ and $7.4 \times 10^{-4}\,\mathrm{psu}^{-1}$ respectively. Because the resolution is insufficient to permit the development of baroclinic

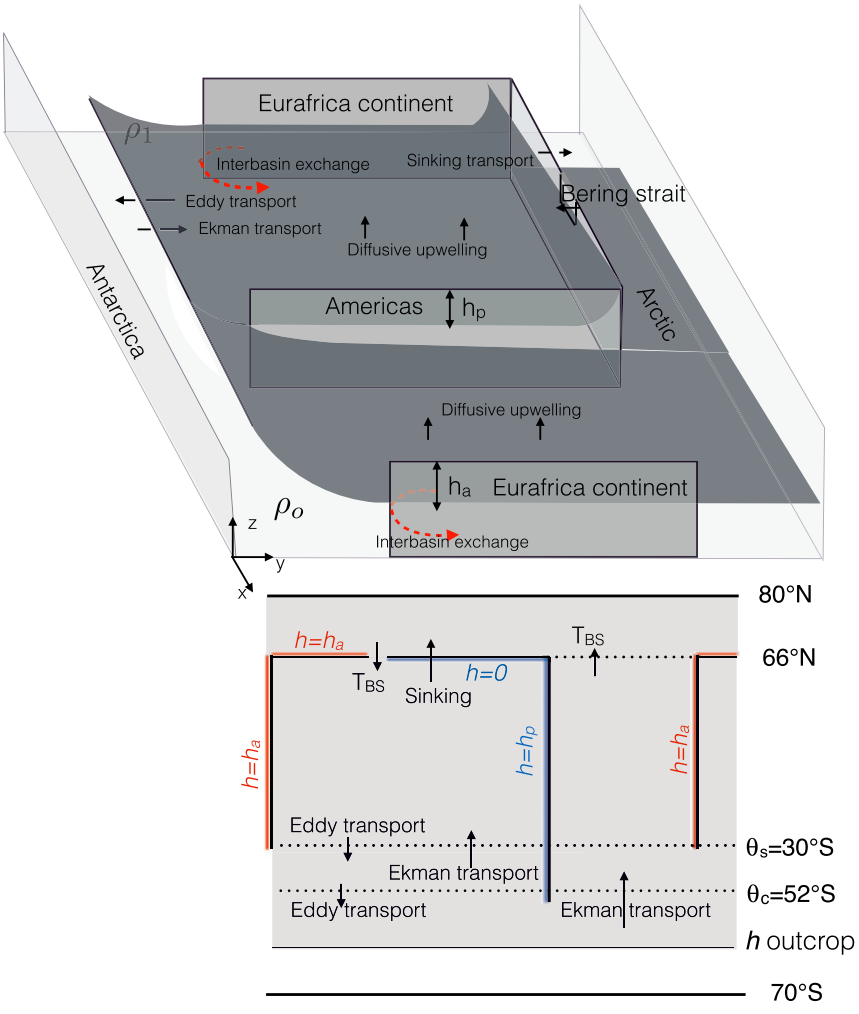

FIG. 5. As in Fig. 2, but that sinking is in the Pacific-like (wide) basin.

eddies, their effect on tracer transport is parameterized using the Gent–McWilliams advective parameterization (Gent and McWilliams 1990; Griffies 1998; Ferrari et al. 2010), and the isopycnal tracer mixing scheme described by Redi (1982), with equal constant coefficients of eddy diffusivity $\kappa_{GM} = \kappa_{Redi} = 500\,m^2\,s^{-1}$. The vertical diffusivity is set to $2 \times 10^{-5}\,m^2\,s^{-1}$ in the interior, increasing to $1 \times 10^{-2}\,m^2\,s^{-1}$ at the surface over a depth of 30 m to model the mixed layer. A simple convective adjustment scheme is used where vertical tracer diffusivity is increased to $10\,m^2\,s^{-1}$ when stratification is statically unstable. Most ocean general circulation models, in addition to a surface mixed layer and a convective adjustment scheme use a diffusivity that increases with depth below 2500 m (Bryan and Lewis 1979; Nikurashin and Ferrari 2013). The bottom-enhanced diapycnal diffusivity is well below the upper branch of the MOC, and while essential for the abyssal circulation, it is subdominant for the middepth circulation (Cessi 2019; Johnson et al. 2019), and is omitted here.

The surface forcing is prescribed as steady zonally uniform wind stress (top panel of Fig. 7), relaxation to a zonally uniform temperature T^*, with a time scale of 15 days (middle panel of Fig. 7), and freshwater flux (virtual salt flux) that is zonally uniform within each sector from 0° to 70°E and from 70° to 210°E, but varies between the two sectors in the latitudinal range from 25° to 66°N, controlling the location of sinking (bottom panel of Fig. 7).

The model is integrated until statistical steady state is achieved, i.e., about 3000 years, starting from initial conditions in a nearby part of parameter space.

a. Varying the surface forcing

One of the main assumptions of the conceptual model is that the depth of the isopycnal separating the northward and southward limbs of the MOC is constant along each

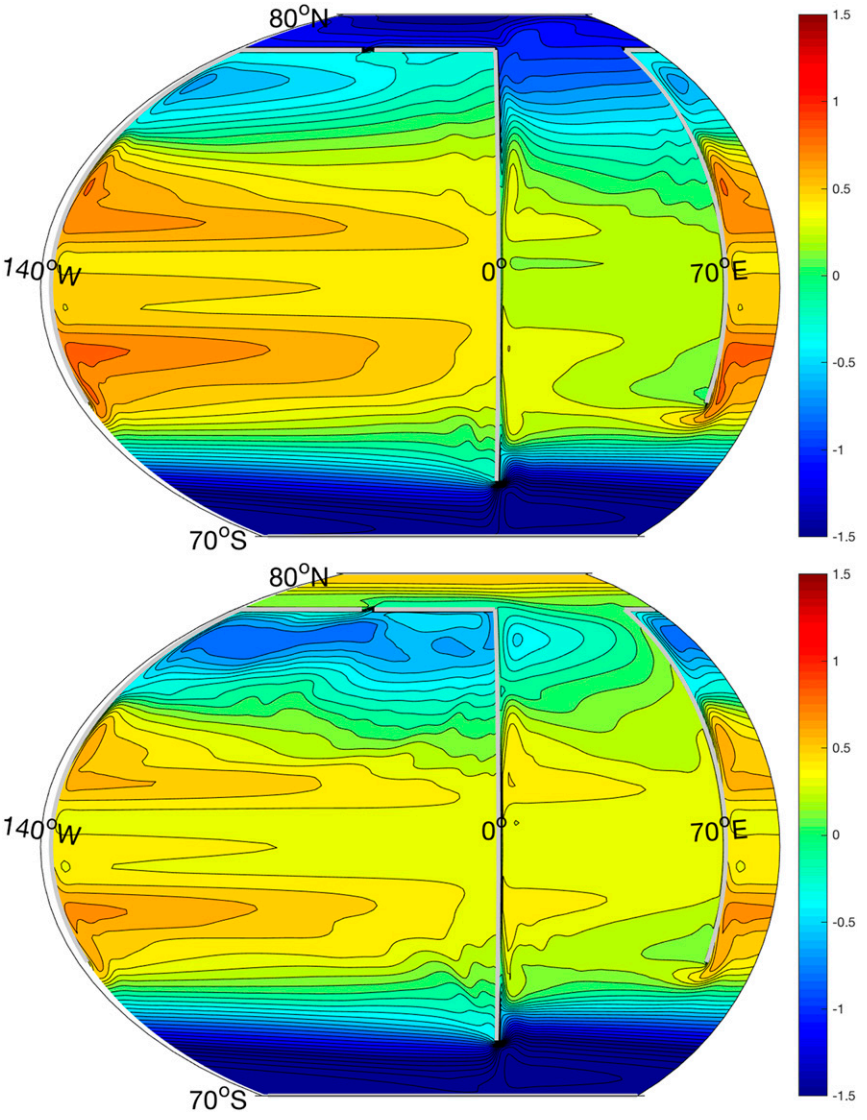

FIG. 6. (top) SSH (m) for a computation with sinking in the narrow basin (''2 winds'' surface wind stress and ''narrow salty–wide fresh'' freshwater flux in Fig. 7). (bottom) SSH (m) for a computation with sinking in the wide basin (''2 winds'' surface wind stress and ''wide salty–narrow fresh'' freshwater flux in Fig. 7). In both panels the solid boundaries are denoted by gray color, and the Bering Strait is 272 km wide (double strait). Notice that SSH is lower in the sinking basin relative to the nonsinking basin. The westernmost 20° of longitude are repeated on the eastern side of the domain to illustrate the 210° periodicity in longitude.

eastern boundary, while outcropping in the sinking sector at the latitude of Bering Strait. The conceptual model predicts that the depth of the isopycnal increases as the circumpolar wind stress increases, and that it is shallower in the sinking basin. The assumptions and predictions are qualitatively confirmed by the numerical simulations in line with previous work without a Bering-like strait (Gnanadesikan 1999; Jones and Cessi 2016; Cessi and Jones 2017). Figure 8 shows the density on the eastern boundary of the narrow basin (Atlantic-like) as a function of latitude and depth for the three wind stress profiles shown in the top panel of Fig. 7, while using the freshwater flux profiles with the black lines in the bottom panel of Fig. 7. In the bottom-right panel of Fig. 8 the freshwater flux is changed to the profiles with the blue lines in the bottom panel of Fig. 7, inducing sinking in the Pacific-like (wide) basin (bottom-right panel). The corresponding densities on the eastern boundary of the Pacific-like (wide) basin are shown in Fig. 9. The main point is that above the separating depth of the MOC (i.e.,

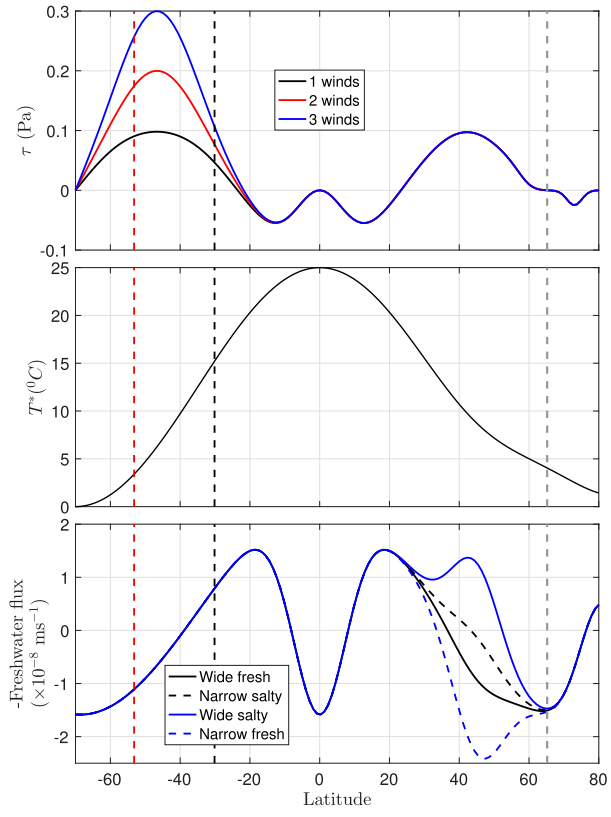

FIG. 7. (top) The different surface wind-stress profiles applied to the MITgcm. (middle) Relaxation temperature T^* to which the model surface temperature is relaxed on a time scale of 15 days. (bottom) The negative surface freshwater flux. The salinity (virtual) flux profiles imposed at the model's surface is the negative of the freshwater flux, multiplied by the reference salinity (35 psu). The black lines show the profiles for sinking in the narrow sector (Atlantic-like): the profile in the narrow sector (0°–70°E) (black solid) and in the wide sector (140°W–0°E) (black dashed), amounting to a 0.13 Sv difference of area-integrated freshwater flux between the two sectors (wide minus narrow). The blue lines show the profiles for sinking in the wide sector (Pacific-like): the profile in the narrow sector (0°–70°E) (blue dashed) and in the wide sector (140°W–0°E) (blue solid), amounting to a −0.58 Sv difference of area integrated freshwater flux between the two sectors (wide minus narrow).

above the isopycnal marked by a thick line) are systematically shallower in the sinking basin, outcropping before or at the latitude of the strait (marked by a white line, bold in the wide basin and dashed in the narrow basin).

The corresponding overturnings are visualized using the zonally and time-averaged residual streamfunction ψ, defined as

$$\psi(y,\tilde{\rho}) \equiv -\frac{1}{TL}\int_0^T dt \int_0^L dx \int_{-H}^0 v^\dagger(x,y,z,t)\,\mathscr{H}[\rho(x,y,z,t) - \tilde{\rho}]\,dz\,. \tag{19}$$

where $T = 100$ years, $v^\dagger = v + v_{\mathrm{GM}}$ is the total meridional velocity (the sum of the resolved velocity v and the eddy velocity from the GM parameterization v_{GM}), and $\mathscr{H}$ is the Heaviside step function; ψ is the zonally integrated transport of water below the isopycnal $\rho(x, y, z, t) = \tilde{\rho}$. The "vertical" coordinate $\tilde{\rho}$ is density; the tilde distinguishes the label of a density surface from the density field (Young 2012). The domain for the zonal integration L can be either the narrow sector (0°–70°E) or the wide sector (140°W–0°E) between the latitudes occupied by the short continent (30°S–66°N), but includes the whole zonal extent elsewhere (i.e., for latitudes north of 66°N or south of 30°S).

For presentation purposes, ψ is remapped into height coordinates using the mean isopycnal height

$$\zeta(y,\tilde{\rho}) \equiv -\frac{1}{TL}\int_0^T dt \int_0^L dx \int_{-H}^0 \mathscr{H}[\rho(x,y,z,t) - \tilde{\rho}]\,dz\,. \tag{20}$$

The residual overturning streamfunction for the forcings corresponding to the density fields in Figs. 8 and 9 is shown in Figs. 10 and 11. The important points are 1) the interhemispheric overturning strength increases with the wind stress in the circumpolar region (Toggweiler and Samuels 1993, 1995; Gnanadesikan 1999; Nikurashin and Vallis 2012) and 2) the interhemispheric overturning is accompanied by an interbasin exchange in the nonsinking basin that is expressed as a southward flow at intermediate depths, and a deeper northward return flow (Ferrari et al. 2017).

The strait transport reverses when the sinking is localized in the wide basin, with a magnitude almost equal and opposite to the case of narrow-basin sinking. The reversal in transport is accompanied by a reversal in the sea surface height gradient across the strait and between the subpolar region of the subbasins, as shown in Fig. 6. This behavior is consistent with that found in more comprehensive climate models (Hu and Meehl 2005; Hu et al. 2008, 2011).

Notice that when the overturning is localized in the narrow basin, sinking occurs both in the basin and in the Arctic-like portion of the domain, where densities are highest, while sinking in the wide basin (bottom-left corners of Figs. 10 and 11) occurs south of the strait at lower densities. With the linear equation of state and constant ocean depth, when sinking is in the narrow basin, the densest water at surface is in the Northern Hemisphere, and abyssal water is formed there. In contrast, when sinking occurs in the wide basin, the densest surface water is in the Southern Hemisphere, and abyssal water is formed there. In the latter case, an abyssal counterclockwise cell exists, which pushes the MOC further up in the water column, as documented in

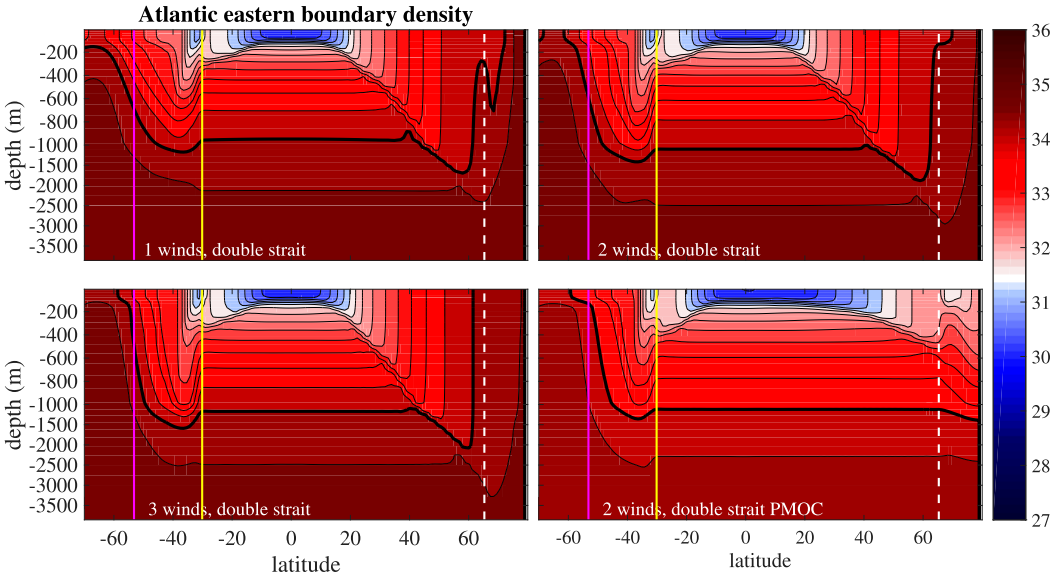

FIG. 8. Time-averaged density anomaly (density $-$ 1000 kg m^{-3}) at the longitude of the eastern boundary of the narrow basin as a function of latitude and depth. The magenta vertical line denotes the southern tip of the long continent, the yellow line is the southern tip of the short continent and the white dashed line is the latitude of the strait. The top-left panel is forced by the wind stress with the black profile (1 winds) in Fig. 7, the top-right panel by the "2 winds" profile, and the bottom-left panel by the "3 winds" profile. These three panels are all forced by the freshwater flux marked by black lines in Fig. 7 (wide fresh–narrow salty), which induces sinking in the narrow basin. The bottom-right panel is forced by the "2 winds" wind stress, and by the freshwater flux marked by blue lines in Fig. 7 (wide salty–narrow fresh), which induces sinking in the wide basin. The contour interval is 0.3 kg m^{-3}. The thick contour denotes the isopycnal approximately separating the upper and lower limbs of the MOC, i.e., the "separating depth."

Jansen and Nadeau (2016). Remarkably, the details of the abyssal cell are irrelevant for Bering Strait transport, whose magnitude is around 3 Sv in all cases.

The increase in overturning is accompanied by an increase in $\Delta\eta$ at the strait, dominated by a large decrease in the SSH on the western and northern side of the strait, i.e., the side determined by the Atlantic dynamics. Figure 12 shows the SSH as a function of arclength along paths following the eastern boundaries of both basins and the northern boundary of the wide basin (moving clockwise for the narrow basin and counterclockwise for the wide basin). For reference, some landmark points along the boundary path are shown in Figs. 12 and 2 (bottom panel). To guarantee continuity of the pressure and SSH, the points on the northern boundary of the narrow basin are evaluated one grid point *north* of the strait's latitude (dashed lines in Fig. 12, corresponding to the red line in Fig. 2), while the points on the northern boundary of the wide basin are evaluated one grid point *south* of the solid boundary (solid lines in Fig. 12, corresponding to the blue line in Fig. 2).

The difference in SSH at the eastern boundaries is almost constant between 30°S and 55°N but increases rapidly as deep isopycnals outcrop in the narrow basin, but not in the wide one. Indeed the isopycnal bounding the upper branch of the MOC from below (thick black contour in Figs. 8 and 9) outcrops at the latitude of Bering Strait in the sinking basin but not in the nonsinking basin (the white line in Figs. 8 and 9 marks the Bering Strait latitude).

The transport across the strait increases with the amplitude of the Southern Hemisphere winds, as shown in Fig. 4, although not as fast as the inviscid model of section 2 predicts. In addition, there is a dependence on the strait width that is not accounted for in the box model.

b. *Varying the strait width*

The conceptual model assumes that the transport and the SSH difference across the strait are in geostrophic balance, independent of the strait width. This assumes that frictional effects are negligible, as appropriate for a strait much larger (and deeper) than a frictional boundary layer width (and depth). This assumption is contrary to a previous theoretical estimate of the Bering Strait flow (Stigebrandt 1984), but it is confirmed by theoretical, numerical, and observational estimates (Toulany and Garrett 1984; Panteleev et al. 2010; Woodgate 2018). In the low-resolution, primitive equation computations, we find that T_{BS} increases slightly with the strait width, shown in Figs. 13 and 14, indicating that the geostrophic estimate is an upper bound for a strait with the actual

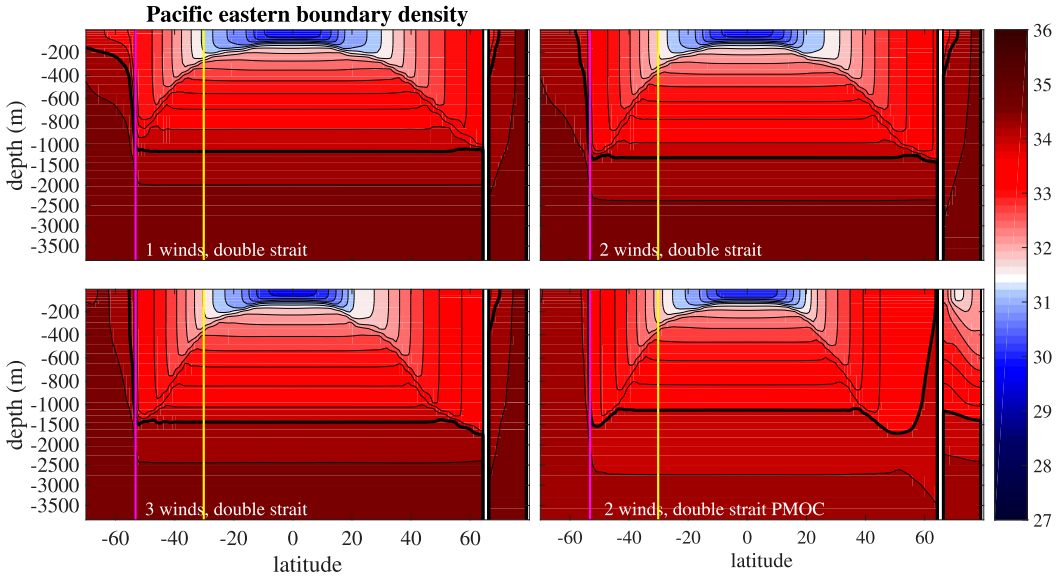

FIG. 9. As in Fig. 8, but for the density on the eastern boundary of the wide basin. Here there is a solid boundary at the latitude of the strait marked by a thick white vertical line.

size of Bering Strait, and that in our model configuration friction becomes important for openings less than 136 km (which is the narrowest considered in our computations). It is possible that a higher-resolution model would not display the same sensitivity as the low-resolution computations.

Other geometrical aspects of the strait, neglected in the simplified model, might contribute to, and mostly decrease, the transport: frictional effects in the shallow shelf on both sides of the strait can break the geostrophic constraint along the coast, effectively decreasing the SSH signal along the northern boundary of the Pacific

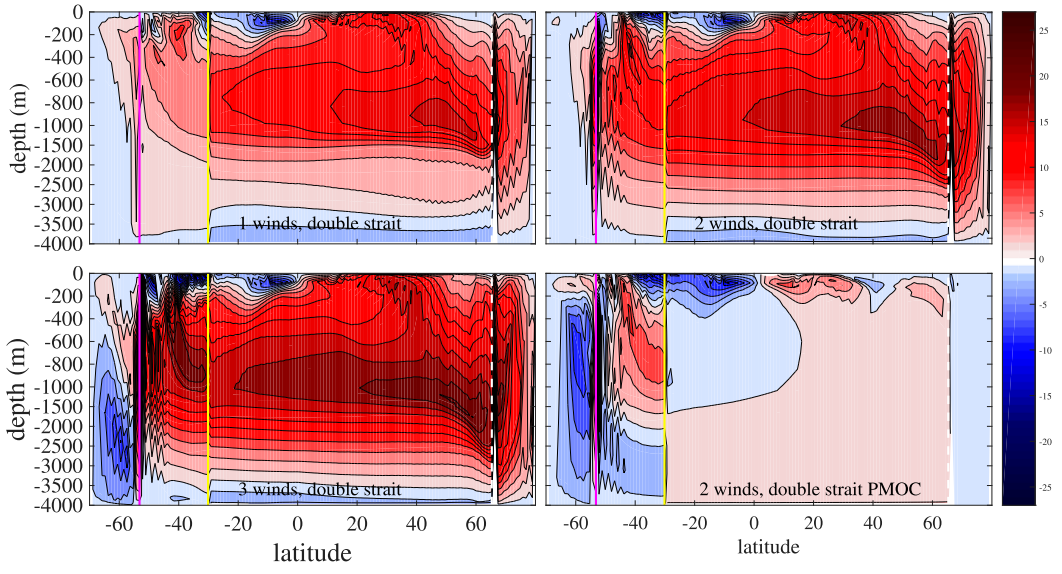

FIG. 10. Time- and zonally averaged residual streamfunction in the narrow basin as a function of latitude and depth. The magenta vertical line denotes the southern tip of the long continent, the yellow line is the southern tip of the short continent, and the white dashed line is the latitude of the strait. The top-left panel is forced by the wind stress with the black profile (1 winds) in Fig. 7, the top-right panel by the "2 winds" profile, and the bottom-left panel by the "3 winds" profile. These three panels are all forced by the freshwater flux marked by black lines in Fig. 7 (wide fresh–narrow salty), which induces sinking in the narrow basin. The bottom-right panel is forced by the "2 winds" wind stress, and by the (wide salty–narrow fresh) freshwater flux, which induces sinking in the wide basin. The contour interval is 2 Sv.

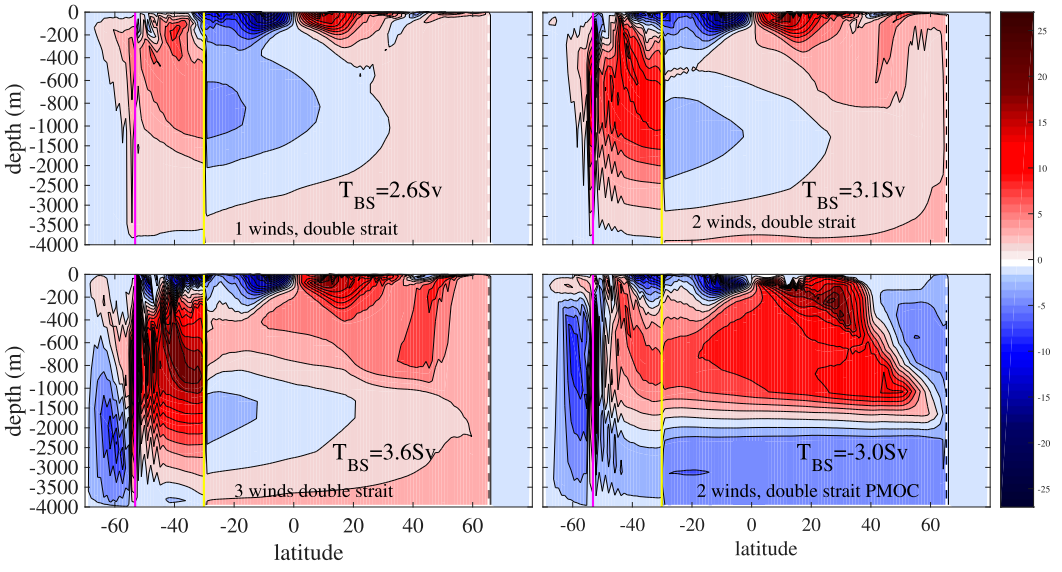

FIG. 11. As in Fig. 10, but for the residual streamfunction in the wide basin. The time-averaged transport across the strait in Sv, T_{BS}, is marked in the bottom-right section of each contour plot.

and the southern boundary of the Arctic. In addition, the pressure and SSH signal can be locally modified by along-strait wind stress in combination with frictional effects on the shallow shelf, by setting up a local sea surface slope across the strait: this is the process that induces a reduced or even reversed transport in the winter months (Woodgate 2018), when there is a strong northerly wind. Finally, there is classical Ekman transport: a net westerly wind stress along the southern boundary of the Arctic would reduce the east–west difference in SSH over the value obtained neglecting the coastal Ekman transport. In summary, it appears that the local effects neglected here, i.e., shallow shelf, friction and local wind, tend to drive a southward flow against the northward Bering Strait transport balanced by the large-scale pressure difference between the North Atlantic and North Pacific.

4. Summary and discussion

We attribute the SSH difference across Bering Strait, which geostrophically balances the associated northward climatological transport, to the large-scale difference in isopycnal depth associated with the MOC. In particular, we focus on the isopycnals that separate the upper and lower limbs of the MOC: these are the isopycnals that outcrop in the North Atlantic and Arctic, and are associated with the formation of North Atlantic Deep Water. The same isopycnals do not outcrop in the North Pacific and this leads to a large-scale difference in isopycnal depths in the northern latitudes of these basins, resulting in a pressure and SSH difference across Bering Strait. The idea that the MOC controls the Bering Strait throughflow has been proposed previously by De Boer and Nof (2004), but not in terms of the relation between the SSH and the

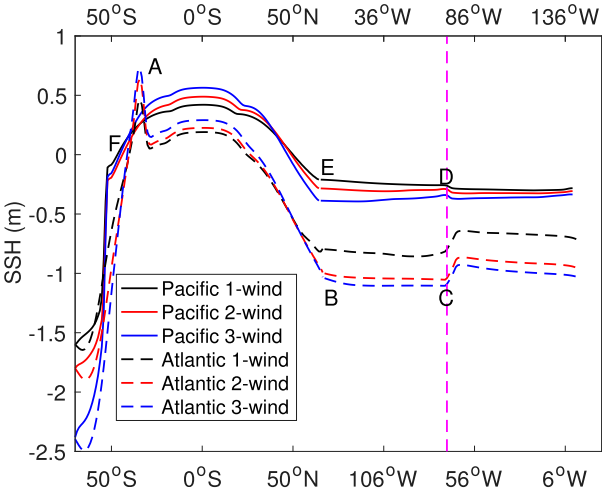

FIG. 12. SSH along the arclengths following the anticlockwise path along the eastern and northern boundaries of the wide basin (solid lines and upper abscissa labels), and the clockwise path along the eastern boundary of the narrow basin and the northern boundary of the wide basin (dashed lines and lower abscissa labels). Along the northern boundary of the wide basin, the path is one grid point south of the strait's latitude, while for the narrow basin the path is evaluated one grid point north of the strait's latitude. The capital letters denote the landmark points marked in the lower panel of Fig. 2. The colors of the lines indicate the strength of the wind stress in the Southern Hemisphere circumpolar region, using the same color scheme as in the top panel of Fig. 7.

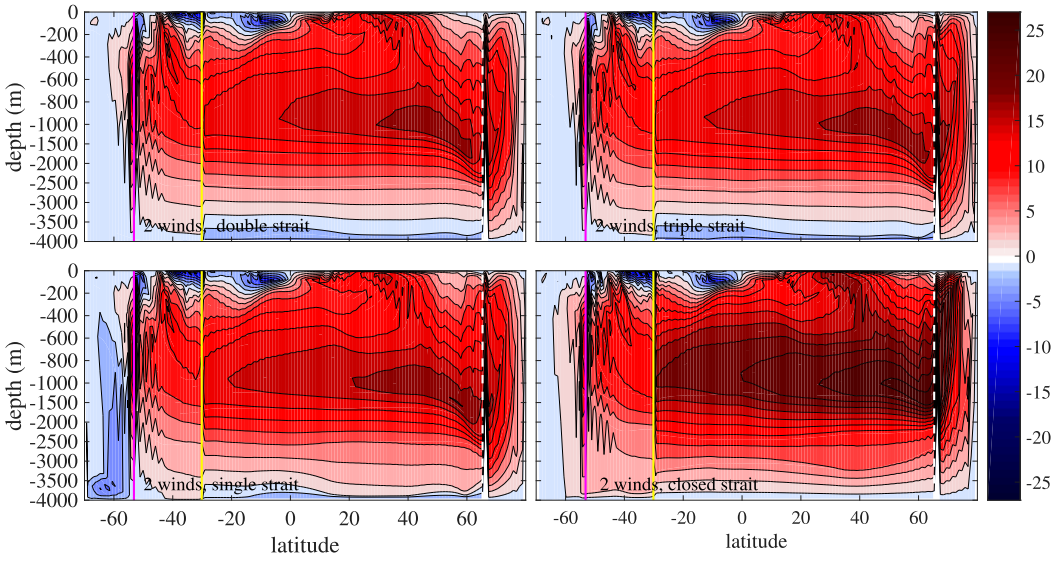

FIG. 13. Time- and zonally averaged residual streamfunction in the narrow basin as a function of latitude and depth. The magenta vertical line denotes the southern tip of the long continent, the yellow line is the southern tip of the short continent and the white dashed line is the latitude of the strait. The bottom-right panel has a closed strait, the bottom-left panel has a 136 km strait (single strait), the top-left panel has a strait 272 km wide (double strait), and the top-right panel a strait 408 km. All panels are forced by the wind stress in the red profile (2 winds) and the freshwater flux marked by black lines in Fig. 7 (wide fresh–narrow salty), which induces sinking in the narrow basin. The contour interval is 2 Sv.

isopycnal difference between the North Atlantic/Arctic and the North Pacific.

This hypothesis is quantified with both a one-and-a-half-layer box model, and a three-dimensional, continuously stratified, primitive equations general circulation model, both in a simplified geometry of the World Ocean. It is remarkable how well the predictions of the one-and-a-half-layer box model agree with those of the MITgcm, contingent on the choice of one parameter, g', which quantifies the range of outcropping buoyancies shared by the Antarctic circumpolar region and the Northern Hemisphere deep water formation region (Wolfe and Cessi 2010). In the three-dimensional computations g' is determined by the dynamics of the MOC

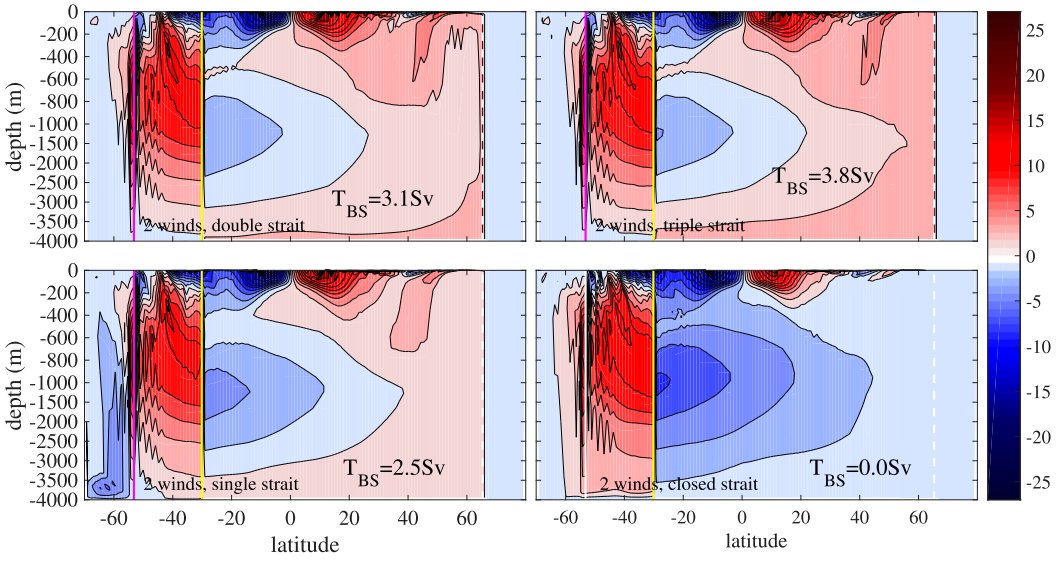

FIG. 14. As in Fig. 10, but for the residual streamfunction in the wide basin. The time-averaged transport across the strait in Sv, T_{BS}, is marked in the bottom-right section of each contour plot.

itself, given the prescription of surface wind stress, surface temperature and surface freshwater flux: because the surface salt flux is prescribed, rather than the surface salinity, the surface buoyancies shared by the sinking region and the Southern Ocean are part of the global solution. Yet, there is quantitative agreement between the one-and-a-half-layer box model and the three-dimensional computations.

Unlike the computations of De Boer and Nof (2004), our model Pacific and Atlantic are connected at high latitudes by circumpolar regions, periodic in longitude rather than bounded by meridional barriers. This is an important detail, especially for the Southern Hemisphere connection, because it is only in a circumpolar geometry that the surface Ekman transport is returned below the bottom topography: in a domain bounded to the East and West the return of the Ekman transport occurs within shallow wind-driven gyres, and there is no middepth stratification and overturning circulation (Wolfe and Cessi 2010).

We show that the Ekman transport in the circumpolar region of the Southern Hemisphere controls the SSH drop across Bering Strait, mediated by the MOC, and we quantify the dependence of the climatological Bering Strait transport on the circumpolar wind stress. The simplified geometry and forcing overestimates the Bering Strait transport: we do not consider the effect of the shallow shelf that surrounds Bering Strait and the associated bottom friction, which would limit the conservation of pressure and SSH along the solid boundaries connecting to the strait, thus reducing the SSH difference across the strait. According to the observations presented in Fig. 1, while the SSH difference between the eastern boundaries of the high-latitude North Atlantic and of the high-latitude North Pacific is about 0.6 m, the SSH difference drops to about 0.2 m across Bering Strait. Almost all of this drop occurs in the Arctic indicating that a substantial attenuation of the SSH signal occurs on the Arctic shelf. In our shelfless model the jump in SSH that occurs across the strait between the Pacific-like region and the Atlantic/Arctic-like region is constant throughout the Arctic's boundary, ranging from 0.6 to 0.8 m depending on the strength of the ACC winds (cf. the SSH difference between the points E and B in Fig. 12). Presumably, as in nature, this difference would be decreased as Bering Strait is approached if a shelf were included.

We also ignore the coastal Ekman transport associated with wind stress anywhere along the southern boundary of the Arctic and along the eastern boundary of the Pacific: this wind stress would alter the SSH difference across Bering Strait. Finally, the local wind stress at Bering Strait is neglected: as detailed in Woodgate (2018) the along strait wind induces a transport parallel to the wind, and thus southward in the prevailing northerlies of this region.

When the prescribed surface freshwater flux is contrived to induce deep water formation in the North Pacific, rather than in the North Atlantic/Arctic, then the difference in SSH across Bering Strait, and the associated transport are reversed. This result is consistent with previously published numerical simulations in a realistic configuration of the World Ocean (Hu and Meehl 2005; Hu et al. 2008, 2011). As in those computations, we find that the sign of the transport is reversed, but the amplitude is the same, consistently with the notion that the strength of the MOC and the middepth stratification is controlled by the wind stress and eddy transport in the Antarctic circumpolar region and by the global diapycnal mixing, regardless of the sinking location. These same processes control the SSH difference between the North Pacific and North Atlantic, and ultimately the climatological sign and amplitude of Bering Strait transport.

Acknowledgments. Support by the National Science Foundation under Grant OCE-1634128 is gratefully acknowledged. Computational resources were provided by the Extreme Science and Engineering Discovery Environment (XSEDE) on Stampede2 at the Texas Advanced Computing Center through allocation TG-OCE130026. XSEDE is supported by the National Science Foundation Grant ACI-1548562.

REFERENCES

Aagaard, K., T. J. Weingartner, S. L. Danielson, R. A. Woodgate, G. C. Johnson, and T. E. Whitledge, 2006: Some controls on flow and salinity in Bering Strait. *Geophys. Res. Lett.*, **33**, L19602, https://doi.org/10.1029/2006GL026612.

Bryan, K., and L. Lewis, 1979: A water mass model of the world ocean. *J. Geophys. Res.*, **84**, 2503–2517, https://doi.org/10.1029/JC084iC05p02503.

Cessi, P., 2019: The global overturning circulation. *Annu. Rev. Mar. Sci.*, **11**, 249–270, https://doi.org/10.1146/annurev-marine-010318-095241.

——, and C. Jones, 2017: Warm-route versus cold-route interbasin exchange in the meridional overturning circulation. *J. Phys. Oceanogr.*, **47**, 1981–1997, https://doi.org/10.1175/JPO-D-16-0249.1.

Danielson, S. L., E. Curchitser, K. Hedstrom, T. Weingartner, and P. Stabeno, 2011: On ocean and sea ice modes of variability in the Bering Sea. *J. Geophys. Res.*, **116**, C12034, https://doi.org/10.1029/2011JC007389.

——, T. J. Weingartner, K. S. Hedstrom, K. Aagaard, R. Woodgate, E. Curchitser, and P. J. Stabeno, 2014: Coupled wind-forced controls of the Bering–Chukchi shelf circulation and the Bering Strait throughflow: Ekman transport, continental shelf waves, and variations of the Pacific–Arctic sea surface height

gradient. *Prog. Oceanogr.*, **125**, 40–61, https://doi.org/10.1016/j.pocean.2014.04.006.

De Boer, A. M., and D. Nof, 2004: The Bering Strait's grip on the Northern Hemisphere climate. *Deep-Sea Res. I*, **51**, 1347–1366, https://doi.org/10.1016/j.dsr.2004.05.003.

Ferrari, R., S. M. Griffies, A. J. G. Nurser, and G. K. Vallis, 2010: A boundary-value problem for the parameterized mesoscale eddy transport. *Ocean Modell.*, **32**, 143–156, https://doi.org/10.1016/j.ocemod.2010.01.004.

——, L.-P. Nadeau, D. P. Marshall, L. C. Allison, and H. L. Johnson, 2017: A model of the ocean overturning circulation with two closed basins and a reentrant channel. *J. Phys. Oceanogr.*, **47**, 2887–2906, https://doi.org/10.1175/JPO-D-16-0223.1.

Forget, G., J.-M. Campin, P. Heimbach, C. N. Hill, R. M. Ponte, and C. Wunsch, 2015: ECCO version 4: An integrated framework for non-linear inverse modeling and global ocean state estimation. *Geosci. Model Dev.*, **8**, 3071–3104, https://doi.org/10.5194/gmd-8-3071-2015.

Fukumori, I., O. Wang, I. Fenty, G. Forget, P. Heimbach, and R. M. Ponte, 2017: ECCO version 4 release 3. 10 pp., http://hdl.handle.net/1721.1/110380.

Gent, P., and J. C. McWilliams, 1990: Isopycnal mixing in ocean circulation models. *J. Phys. Oceanogr.*, **20**, 150–155, https://doi.org/10.1175/1520-0485(1990)020<0150:IMIOCM>2.0.CO;2.

Gill, A., and P. Niller, 1973: The theory of the seasonal variability in the ocean. *Deep-Sea Res. Oceanogr. Abstr.*, **20**, 141–177, https://doi.org/10.1016/0011-7471(73)90049-1.

Gnanadesikan, A., 1999: A simple predictive model for the structure of the oceanic pycnocline. *Science*, **283**, 2077–2079, https://doi.org/10.1126/science.283.5410.2077.

Godfrey, J., 1989: A Sverdrup model of the depth-integrated flow for the world ocean allowing for island circulations. *Geophys. Astrophys. Fluid Dyn.*, **45**, 89–112, https://doi.org/10.1080/03091928908208894.

Griffies, S. M., 1998: The Gent–McWilliams skew flux. *J. Phys. Oceanogr.*, **28**, 831–841, https://doi.org/10.1175/1520-0485(1998)028<0831:TGMSF>2.0.CO;2.

Hu, A., and G. A. Meehl, 2005: Bering Strait throughflow and the thermohaline circulation. *Geophys. Res. Lett.*, **32**, L24610, https://doi.org/10.1029/2005GL024424.

——, B. L. Otto-Bliesner, G. A. Meehl, W. Han, C. Morrill, E. C. Brady, and B. Briegleb, 2008: Response of thermohaline circulation to freshwater forcing under present-day and LGM conditions. *J. Climate*, **21**, 2239–2258, https://doi.org/10.1175/2007JCLI1985.1.

——, G. A. Meehl, W. Han, and J. Yin, 2011: Effect of the potential melting of the Greenland Ice Sheet on the meridional overturning circulation and global climate in the future. *Deep-Sea Res. II*, **58**, 1914–1926, https://doi.org/10.1016/j.dsr2.2010.10.069.

Jansen, M. F., and L.-P. Nadeau, 2016: The effect of Southern Ocean surface buoyancy loss on the deep-ocean circulation and stratification. *J. Phys. Oceanogr.*, **46**, 3455–3470, https://doi.org/10.1175/JPO-D-16-0084.1.

Johnson, H. L., P. Cessi, D. P. Marshall, F. Schloesser, and M. A. Spall, 2019: Recent contributions of theory to our understanding of the Atlantic Meridional Overturning Circulation. *J. Geophys. Res. Oceans*, **124**, 5376–5399, https://doi.org/10.1029/2019JC015330.

Jones, C. S., and P. Cessi, 2016: Interbasin transport of the meridional overturning circulation. *J. Phys. Oceanogr.*, **46**, 1157–1169, https://doi.org/10.1175/JPO-D-15-0197.1.

Kinney, J. C., and Coauthors, 2014: On the flow through Bering Strait: A synthesis of model results and observations. *The Pacific Arctic Region*, J. Grebmeier and W. Maslowski, Eds., Springer, 167–198, https://doi.org/10.1007/978-94-017-8863-2_7.

Marshall, J., and T. Radko, 2003: Residual-mean solutions for the Antarctic Circumpolar Current and its associated overturning circulation. *J. Phys. Oceanogr.*, **33**, 2341–2354, https://doi.org/10.1175/1520-0485(2003)033<2341:RSFTAC>2.0.CO;2.

——, C. Hill, L. Perelman, and A. Adcroft, 1997: Hydrostatic, quasi-hydrostatic, and nonhydrostatic ocean modeling. *J. Geophys. Res.*, **102**, 5733–5752, https://doi.org/10.1029/96JC02776.

Maslowski, W., D. Marble, W. Walczowski, U. Schauer, J. L. Clement, and A. J. Semtner, 2004: On climatological mass, heat, and salt transports through the Barents Sea and Fram Strait from a pan-Arctic coupled ice-ocean model simulation. *J. Geophys. Res.*, **109**, C03032, https://doi.org/10.1029/2001JC001039.

Nguyen, A. T., D. Menemenlis, and R. Kwok, 2011: Arctic ice-ocean simulation with optimized model parameters: Approach and assessment. *J. Geophys. Res.*, **116**, C04025, https://doi.org/10.1029/2010JC006573.

Nikurashin, M., and G. Vallis, 2012: A theory of the interhemispheric meridional overturning circulation and associated stratification. *J. Phys. Oceanogr.*, **42**, 1652–1667, https://doi.org/10.1175/JPO-D-11-0189.1.

——, and R. Ferrari, 2013: Overturning circulation driven by breaking internal waves in the deep ocean. *Geophys. Res. Lett.*, **40**, 3133–3137, https://doi.org/10.1002/grl.50542.

Panteleev, G., D. A. Nechaev, A. Proshutinsky, R. Woodgate, and J. Zhang, 2010: Reconstruction and analysis of the Chukchi Sea circulation in 1990–1991. *J. Geophys. Res.*, **115**, C08023, https://doi.org/10.1029/2009JC005453.

Redi, M. H., 1982: Oceanic isopycnal mixing by coordinate rotation. *J. Phys. Oceanogr.*, **12**, 1154–1158, https://doi.org/10.1175/1520-0485(1982)012<1154:OIMBCR>2.0.CO;2.

Reid, J. L., 1961: On the temperature, salinity, and density differences between the Atlantic and Pacific Oceans in the upper kilometre. *Deep-Sea Res.*, **7**, 265–275, https://doi.org/10.1016/0146-6313(61)90044-2.

Stigebrandt, A., 1984: The North Pacific: A global-scale estuary. *J. Phys. Oceanogr.*, **14**, 464–470, https://doi.org/10.1175/1520-0485(1984)014<0464:TNPAGS>2.0.CO;2.

Sumata, H., and A. Kubokawa, 2001: Numerical study of eastern boundary ventilation and its effects on the thermocline structure. *J. Phys. Oceanogr.*, **31**, 3002–3019, https://doi.org/10.1175/1520-0485(2001)031<3002:NSOEBV>2.0.CO;2.

Thompson, A. F., A. L. Stewart, and T. Bischoff, 2016: A multi-basin residual-mean model for the global overturning circulation. *J. Phys. Oceanogr.*, **46**, 2583–2604, https://doi.org/10.1175/JPO-D-15-0204.1.

Toggweiler, J. R., and B. Samuels, 1993: Is the magnitude of the deep outflow from the Atlantic Ocean actually governed by Southern Hemisphere winds? *The Global Carbon Cycle*, M. Heimann, Ed., NATO ASI Series, Vol. I, Springer, 333–366.

——, and ——, 1995: Effect of Drake Passage on the global thermohaline circulation. *Deep-Sea Res. I*, **42**, 477–500, https://doi.org/10.1016/0967-0637(95)00012-U.

Toulany, B., and C. Garrett, 1984: Geostrophic control of fluctuating barotropic flow through straits. *J. Phys. Oceanogr.*, **14**,

649–655, https://doi.org/10.1175/1520-0485(1984)014<0649:GCOFBF>2.0.CO;2.

Wolfe, C. L., and P. Cessi, 2010: What sets the strength of the mid-depth stratification and overturning circulation in eddying ocean models? *J. Phys. Oceanogr.*, **40**, 1520–1538, https://doi.org/10.1175/2010JPO4393.1.

Woodgate, R. A., 2018: Increases in the Pacific inflow to the Arctic from 1990 to 2015, and insights into seasonal trends and driving mechanisms from year-round Bering Strait mooring data. *Prog. Oceanogr.*, **160**, 124–154, https://doi.org/10.1016/j.pocean.2017.12.007.

Young, W. R., 2012: An exact thickness-weighted average formulation of the Boussinesq equations. *J. Phys. Oceanogr.*, **42**, 692–707, https://doi.org/10.1175/JPO-D-11-0102.1.

Zhang, J., R. Woodgate, and R. Moritz, 2010: Sea ice response to atmospheric and oceanic forcing in the Bering Sea. *J. Phys. Oceanogr.*, **40**, 1729–1747, https://doi.org/10.1175/2010JPO4323.1.